

Numerical Modeling of Eccentered LWD Borehole Sensors in Dipping and Fully-Anisotropic Earth Formations

Hwa Ok Lee, Fernando L. Teixeira, Luis E. San Martin, and Michael S. Bittar

Abstract—Logging-while-drilling (LWD) borehole sensors are used to provide real-time resistivity data of adjacent Earth formations for hydrocarbon exploration. This allows for an proactive adjustment of the dipping angle and azimuth direction of the drill, and hence geosteering capabilities. The analysis of borehole eccentricity effects on LWD sensor response in full 3×3 anisotropic Earth formations is important for correct data interpretation in deviated or horizontal wells. In this paper, we present a cylindrical-grid finite-difference time-domain (FDTD) model to tackle this problem. The grid is aligned to the sensor axis to avoid staircasing error in the sensor geometry, but in general misaligned to the (eccentered) borehole/formation interface. A locally-conformal discretization is used to compute effective conductivity tensors of partially-filled grid cells at those interfaces, involving an isotropic medium (borehole) and a full 3×3 anisotropic medium in general (dipped Earth formation). The numerical model is used to compute the response of eccentered LWD sensors in layered Earth formations with anisotropic dipping beds.

Index Terms—Anisotropic media, FDTD methods, geophysical exploration, well-loggng.

I. INTRODUCTION

LOGGING-while-drilling (LWD) sensors are widely used in real-time borehole measurements of petrophysical parameters for hydrocarbon exploration. LWD sensors can provide estimates for electrical conductivity (resistivity) of the Earth formation surrounding the borehole, one of the basic indicators of the concentration of hydrocarbon saturation. In a macroscopic description, these conductivities are anisotropic because of geological factors such as the presence of sand and clay laminates with directional resistivities or the presence of salt water in fractured porous formations (leading to an increase in the conductivity in the direction of fracture). During deviated or horizontal drilling, the Earth anisotropy is represented by a full 3×3 tensor (as opposed to a diagonal tensor in typical vertical drilling scenarios) in a coordinate system aligned with the sensor axis [1]- [3]. Also during deviated/horizontal drilling, the logging sensor may becomes eccentered with respect to the borehole axis because

Manuscript received MM DD, YYYY; revised MM DD, YYYY.

This work was supported in part by Halliburton and by OSC through grants PAS-0061 and PAS-0110.

H. O. Lee and F. L. Teixeira are with ElectroScience Laboratory, Department of Electrical and Computer Engineering, The Ohio State University, Columbus, Ohio 43210, USA (email: teixeira@ece.osu.edu).

L. E. San Martin is with the Sensor Physics Group, Halliburton Energy Services, Houston, Texas 77032, USA.

M. S. Bittar is with Dhahran Technology Center for Middle East and North Africa, Halliburton Energy Services, Dhahran, Saudi Arabia.

of gravitational pull [4] (in general, eccentricity may also result from mechanical vibration). Analysis of the *combined* effect of anisotropy and eccentricity is important for understanding measurements in deviated wells and for the eventual design of new LWD sensors for extracting relevant logging data such as resistivity anisotropy, bed proximity, and dipping angle.

Various numerical methods have been applied over the years to study the response of LWD sensors in complex environments [5]- [24], including eccentered boreholes [12] or full 3×3 anisotropic formations [17], [20], [22], [23]. The finite-difference time-domain (FDTD) method, in particular, is very attractive to analyze LWD sensors in complex environments due to its flexibility to model arbitrarily heterogeneous Earth formations and relative ease of implementation. Furthermore, FDTD is matrix-free algorithm that is massively parallelizable [25]. Due to the cylindrical geometry of LWD sensors, FDTD models employing cylindrical grids aligned with the sensor axis (as opposed to the conventional FDTD based on a Cartesian grid) are instrumental in reducing the discretization error. However, in simulations involving eccentered boreholes, partially-filled grid cells are still present at the borehole/formation interface, which is non-conformal to the cylindrical grid. Locally-conformal FDTD algorithms based on edge-based or face-based approximations for effective conductivities [26]- [28] have been used to model such partially-filled cells [12], [24]. For interfaces between isotropic media, approaches based on effective conductivities are attractive because they preserve the conditional stability of FDTD and can be implemented without major modifications on the FDTD algorithm. However, these approaches are less suited for interfaces involving full 3×3 anisotropic media, where they produce numerical instabilities. More recently, an alternative locally-conformal FDTD approach for full 3×3 anisotropic interfaces was introduced in [29] to compute the *effective* conductivity tensor elements in a consistent fashion based on a quasi-static approximation.

In this paper, we describe the modeling of LWD sensors in eccentered boreholes penetrating through full 3×3 anisotropic formations based on a three-dimensional cylindrical FDTD algorithm. We note that the algorithm described in [17] handled anisotropic media but did not model eccentricity. On the other hand, the algorithm of reference [12] used a face-based on edge-based approximation to model eccentricity but did not handle anisotropy. In the present paper, both full 3×3 anisotropy and borehole eccentricity are handled simultaneously. Furthermore, the eccentricity is modeled in a

more accurate fashion using effective conductivities computed by a quasi-static approximation. The proposed FDTD model is applied to extract the response of eccentered LWD sensors in layered Earth formations with anisotropic-dipping beds, under different combinations of eccentricity offsets and dipping angles.

This paper is organized as follows. In Section II, we describe basic aspects of the numerical formulation, including the representation of anisotropic conductivity tensors in the cylindrical FDTD grid as a function of the dipping angle, the 3-D FDTD leap-frog update (“marching-on-time”) algorithm extended to full 3×3 anisotropic conductive media, and the quasi-static computation of the effective conductivity tensor elements at the eccentered borehole/formation interface. In Section III, we present a series of numerical results, including validation results. In section IV, we briefly summarize the main conclusions.

II. NUMERICAL FORMULATION

Fig. 1 illustrates the geometry of a typical LWD sensor in a borehole crossing a layered Earth formation with a dipping bed. The LWD sensor shown consists of three coil antennas (one transmitter, two receivers) wrapped around a steel mandrel. The mandrel and borehole axes (denoted as z and z' , resp.) in general do not coincide.

A. Deviated wells and full 3×3 anisotropic formations

The Earth conductivity can be expressed as diagonal tensor in a Cartesian system aligned to the vertical Earth direction given by

$$\bar{\sigma}^0 = \begin{bmatrix} \sigma_h & 0 & 0 \\ 0 & \sigma_h & 0 \\ 0 & 0 & \sigma_v \end{bmatrix} \quad (1)$$

where σ_h and σ_v are the horizontal and vertical conductivities, respectively. In general, however, the drilling does not always occur in the vertical direction and deviated or horizontal wells can occur. In this case, the logging sensor ceases to be aligned to the vertical direction. We denote the angle between the vertical direction and the sensor z axis by θ , as indicated in Fig. 1, and choose a cylindrical coordinate system (ρ, ϕ, z) aligned to the sensor axis for the grid discretization. In this coordinate system, the diagonal conductivity tensor $\bar{\sigma}^0$ is transformed to a full tensor $\bar{\sigma}^a$ given by [17]

$$\bar{\sigma}^a = \begin{bmatrix} \sigma_{\rho\rho}^a & \sigma_{\rho\phi}^a & \sigma_{\rho z}^a \\ \sigma_{\phi\rho}^a & \sigma_{\phi\phi}^a & \sigma_{\phi z}^a \\ \sigma_{z\rho}^a & \sigma_{z\phi}^a & \sigma_{zz}^a \end{bmatrix} \quad (2)$$

with

$$\begin{aligned} \sigma_{\rho\rho}^a &= \sigma_\rho \cos^2 \phi + \sigma_\phi \sin^2 \phi \\ \sigma_{\rho\phi}^a &= -\sigma_\rho \sin \phi \cos \phi + \sigma_\phi \sin \phi \cos \phi \\ \sigma_{\rho z}^a &= (\sigma_v - \sigma_h) \cos \phi \sin \theta \cos \theta \\ \sigma_{\phi\rho}^a &= -\sigma_\rho \cos \phi \sin \phi + \sigma_\phi \sin \phi \cos \phi \\ \sigma_{\phi\phi}^a &= \sigma_\rho \sin^2 \phi + \sigma_\phi \cos^2 \phi \\ \sigma_{\phi z}^a &= -(\sigma_v - \sigma_h) \sin \phi \sin \theta \cos \theta \\ \sigma_{z\rho}^a &= (\sigma_v - \sigma_h) \cos \phi \sin \theta \cos \theta \\ \sigma_{z\phi}^a &= -(\sigma_v - \sigma_h) \sin \phi \sin \theta \cos \theta \\ \sigma_{zz}^a &= \sigma_h \sin^2 \theta + \sigma_v \cos^2 \theta \end{aligned} \quad (3)$$

and

$$\begin{aligned} \sigma_\rho &= \sigma_h \cos^2 \theta + \sigma_v \sin^2 \theta \\ \sigma_\phi &= \sigma_h \end{aligned} \quad (4)$$

Note that for $\theta \neq 0$, the tensor elements are functions of position even for a homogeneous layer (i.e., a layer with uniform σ_v and σ_h).

B. Effective conductivities of cut-cells in a cylindrical grid

Fig. 2 illustrates the horizontal cross-section of the geometry. The eccentered interface indicated between the borehole and the formation is nonconformal to the cylindrical grid. This interface cuts through “partially-filled” cells in the cylindrical FDTD grid. We employ a quasi-static approximation to compute effective conductivities and approximate them as uniformly-filled cells. This approximation works well because the dimensions of the grid cells are much smaller than the wavelength of operation. Note that the cells are composed of an isotropic conductivity (borehole region) and, in general, an anisotropic conductivity (Earth formation). Therefore, the effective conductivity is, in general, represented by an anisotropic tensor.

Recall that effective conductance σ^{eff} of a cylinder of length ℓ made of a parallel arrangement of conductivities σ_1 and σ_2 pertaining to cross-section areas A_1 and A_2 , is given by the weighted average $\sigma^{eff} A/\ell = \sigma_1 A_1/\ell + \sigma_2 A_2/\ell$. For a series arrangement, we have $\ell/\sigma^{eff} A = \ell_1/\sigma_1 A + \ell_2/\sigma_2 A$. These basic relations form the basis for the derivation of local effective conductivity tensors $\bar{\sigma}^{eff}$ in Ohm’s law $\mathbf{J} = \bar{\sigma}^{eff} \cdot \mathbf{E}$, for the four possible geometries of partially-filled FDTD cells illustrated in Fig. 3. Assuming cylindrical cells of small enough size, the derivation of effective conductivities for partially-filled cells in a cylindrical grid follows steps analogous to those detailed for a regular (Cartesian) grid in [29]. For brevity, only the final expressions are presented here.

1) *Through-cut cells:* Consider the cut-cell geometry illustrated in Fig. 3(a), where the white volume corresponds to the isotropic borehole region with conductivity σ^i and the green volume to the anisotropic Earth formation. We assume cylindrical cut-cells of size such that we can neglect the cell curvature in the (ρ, ϕ) plane and any difference between the face areas transverse to the radial direction. In other words, each cell can be well approximated by a right quadrilateral frustum. This is typically met in practice as $\Delta\rho/\rho \ll 1$ and

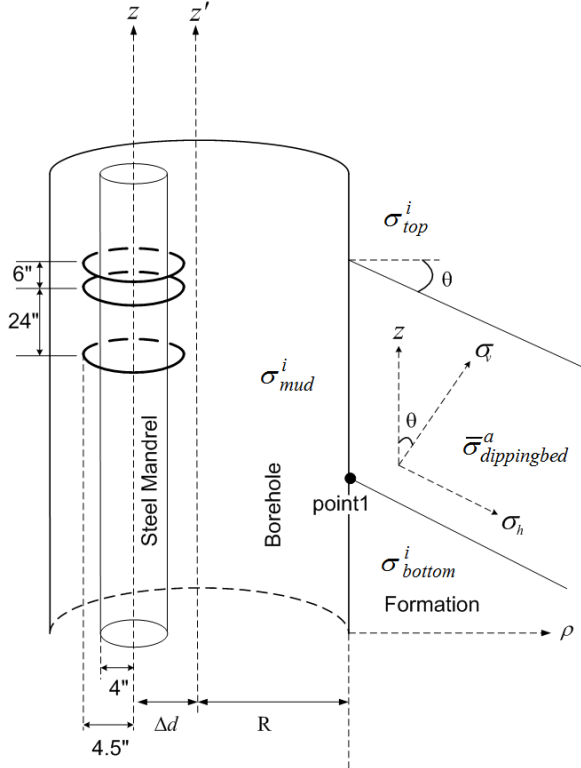


Fig. 1. Illustration of an eccentered LWD sensor consisting of a cylindrical metallic mandrel and three coil antennas crossing a three-layer Earth formation with an anisotropic dipping bed. The "point-1" is a reference point for the logging traces shown later.

$\Delta\phi \ll 2\pi$, where $\Delta\rho$ and $\Delta\phi$ are the spatial discretization steps in the region of interest, see a typical grid scale illustrated in Fig. 4. To derive the effective conductivities $\sigma_{\rho\rho}^{eff}$, $\sigma_{\rho\phi}^{eff}$ and $\sigma_{\rho z}^{eff}$, the equivalent conductances of the partially filled cell shown in Fig. 2(a) are obtained from parallel connection after a series connection of two different conductivity regions with non-uniform lengths. This gives

$$\sigma_{\rho u}^{eff} = \sigma^i \sigma_{\rho u}^a \frac{\Delta\rho}{a} \ln \left(\frac{a+b}{b} \right) \quad (5)$$

where $u = \{\rho, \phi, z\}$, and with $a = (\Delta\rho_1^\ell - \Delta\rho_1^r)(\sigma_{\rho u}^a - \sigma^i)$ and $b = \sigma_{\rho u}^a \Delta\rho_1^r + \sigma^i(\Delta\rho - \Delta\rho_1^r)$. The geometric parameters $\Delta\rho$, $\Delta\rho_1^r$, $\Delta\rho_1^\ell$ are indicated in Fig. 3(a).

Effective conductivities $\sigma_{\phi\rho}^{eff}$, $\sigma_{\phi\phi}^{eff}$ and $\sigma_{\phi z}^{eff}$ are obtained by considering a series connection after a parallel connection of two different conductivity regions with nonuniform cross-section. They are given by

$$\sigma_{\phi u}^{eff} = \frac{1}{A^\phi} \frac{a}{b} \ln \left(\frac{a+b}{b} \right) \quad (6)$$

with $a = (\sigma^i - \sigma_{\phi u}^a)(A_1^{\phi\ell} - A_1^{\phi r})$, with $b = \sigma^i A_1^{\phi r} + \sigma_{\phi u}^a A_2^{\phi r}$, $A_1^{\phi\ell}$ and $A_1^{\phi r}$ being the cross-section areas over the isotropic region on the left- and right-side of the cell, resp. (the right-side is the one visible in the figure), and similarly for $A_2^{\phi\ell}$ and $A_2^{\phi r}$ over the anisotropic region. Furthermore, $A^\phi = A_1^{\phi r} + A_2^{\phi r} = A_1^{\phi\ell} + A_2^{\phi\ell}$.

Effective conductivities $\sigma_{z\rho}^{eff}$, $\sigma_{z\phi}^{eff}$ and σ_{zz}^{eff} are simply obtained by the parallel connection of two uniformly filled

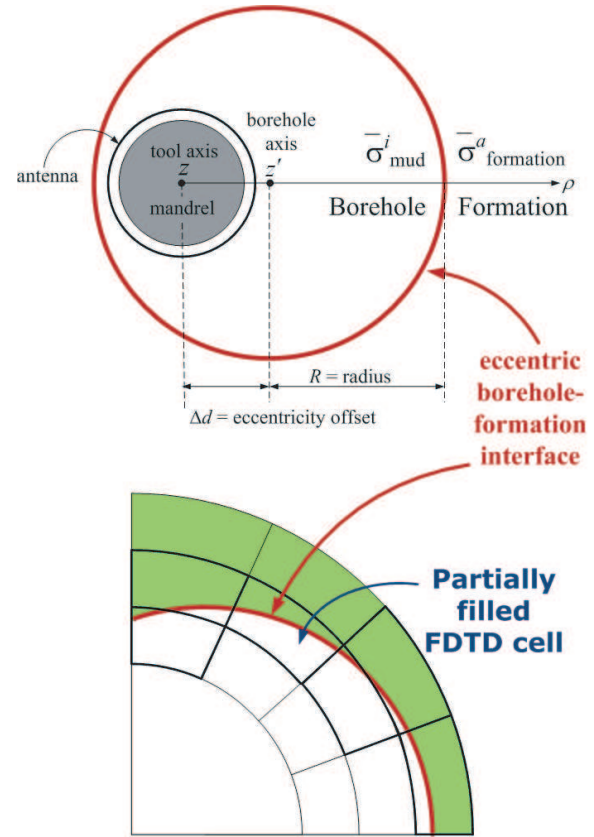


Fig. 2. (Top:) Cross-section of an eccentered LWD sensor configuration and (bottom:) illustration of the non-conformal borehole/formation interface producing partially-filled (cut-cells) on the FDTD grid. The grid cell sizes and the effect are exaggerated for illustration purposes.

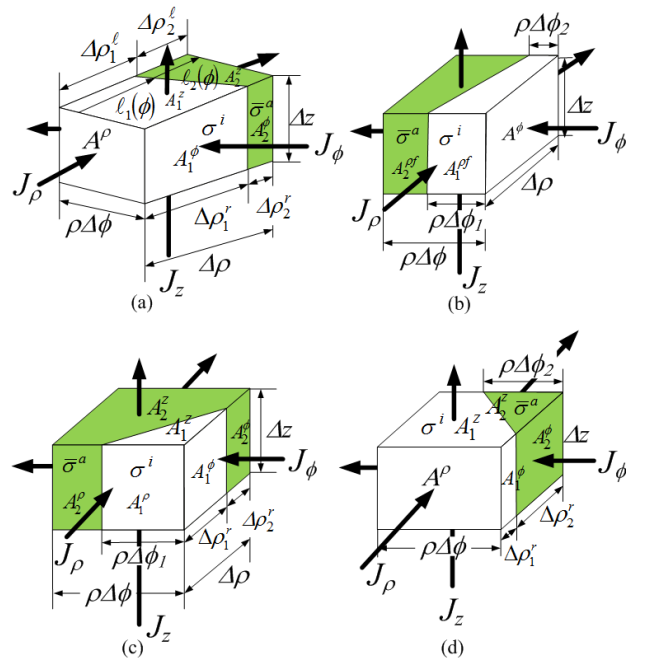


Fig. 3. Four possible geometries for modeling partially filled FDTD cells along an eccentered borehole/formation interface between an isotropic conductivity $\bar{\sigma}^i$ and anisotropic conductivity tensor $\bar{\sigma}^a$.

regions with areas A_1^z (isotropic) and A_2^z (anisotropic) as indicated in Fig. 3(a). Hence, we have

$$\sigma_{zu}^{eff} = \frac{\sigma^i A_1^z + \sigma_{zu}^a A_2^z}{A^z} \quad (7)$$

where $A^z = A_1^z + A_2^z = \rho \Delta\phi \Delta\rho$, and $A_1^z = \rho \Delta\phi \Delta\rho_1^\ell + \rho \Delta\phi (\Delta\rho_1^r - \Delta\rho_1^\ell)/2$.

The effective conductivities $\sigma_{\rho u}^{eff}$ and $\sigma_{\phi u}^{eff}$ for the geometry shown in Fig. 3(b) can be written from the previous expressions by a proper exchange of ρ and ϕ indices, and the left/right indices by front/back indices in the corresponding geometric parameters (expressions for the σ_{zu}^{eff} remain the same).

2) *Side-cut cells*: For the geometries illustrated in Fig. 3(c) and Fig. 3(d), the material interface cuts through adjacent instead of opposite grid faces. Let us consider first effective conductivities for Fig. 3(c). This cell can be seen as a series connection of a homogeneous part with anisotropic conductivity tensor $\bar{\sigma}^a$ only and an inhomogeneous part with a through-cut geometry. The elements of the effective conductivity tensor can therefore be obtained in two steps. In the first step, we follow the same procedure outlined for through-cut cells above, with effective conductivities $\sigma_{\rho\rho(1)}^{eff}$, $\sigma_{\rho\phi(1)}^{eff}$ and $\sigma_{\rho z(1)}^{eff}$ given by

$$\sigma_{\rho u(1)}^{eff} = \frac{1}{A^\rho} \frac{a}{\ln(\frac{a+b}{b})} \quad (8)$$

with $a = A_1^{\rho f} (\sigma_{\rho u}^a - \sigma^i)$ and $b = \sigma^i A_1^{\rho f} + \sigma_{\rho u}^a A_2^{\rho f}$ as before. The second step combines $\sigma_{\rho u(1)}^{eff}$ with the uniform conductivity region in a series connection along ρ . We then have

$$\sigma_{\rho u}^{eff} = \frac{\sigma_{\rho u(1)}^{eff} \sigma_{\rho u}^a \Delta\rho}{\sigma_{\rho u}^a \Delta\rho_1^r + \sigma_{\rho u(1)}^{eff} (\Delta\rho - \Delta\rho_1^r)} \quad (9)$$

Following similar two steps, the effective conductivities $\sigma_{\phi\rho}^{eff}$, $\sigma_{\phi\phi}^{eff}$ and $\sigma_{\phi z}^{eff}$ are expressed as

$$\sigma_{\phi u}^{eff} = \frac{\sigma_{\phi u(1)}^{eff} \sigma_{\phi u}^a \Delta\phi}{\sigma_{\phi u}^a \Delta\phi_1 + \sigma_{\phi u(1)}^{eff} (\Delta\phi - \Delta\phi_1)} \quad (10)$$

where

$$\sigma_{\phi u(1)}^{eff} = \frac{1}{A^\phi} \frac{a}{\ln(\frac{a+b}{b})} \quad (11)$$

with $a = A_1^{\phi r} (\sigma_{\phi u}^a - \sigma^i)$ and $b = \sigma^i A_1^{\phi r} + \sigma_{\phi u}^a A_2^{\phi r}$. Again, the expressions for effective conductivities σ_{zp}^{eff} , $\sigma_{z\phi}^{eff}$ and σ_{zz}^{eff} are not changed from before.

The effective conductivities $\sigma_{\rho u}^{eff}$ and $\sigma_{\phi u}^{eff}$ for the geometry shown in Fig. 3(d) can be written from the above expressions for the geometry of Fig. 3(c) by a proper exchange of ρ and ϕ indices, and left/right indices by front/back indices in the corresponding geometric parameters (expressions for the σ_{zu}^{eff} once more remain the same).

Fig. 4 illustrates an actual example for the distribution of the effective conductivity $\sigma_{\phi\rho}^{eff}$ at an interface between a borehole with isotropic conductivity of $\sigma_{mud} = 0.0005$ S/m (oil-based borehole mud) and an Earth formation with 3×3 anisotropic conductivity with $\sigma_h = 10$ S/m, $\sigma_v = 2.5$ and $\theta = 45^\circ$ in invariant ϕ -direction. The radius of the borehole

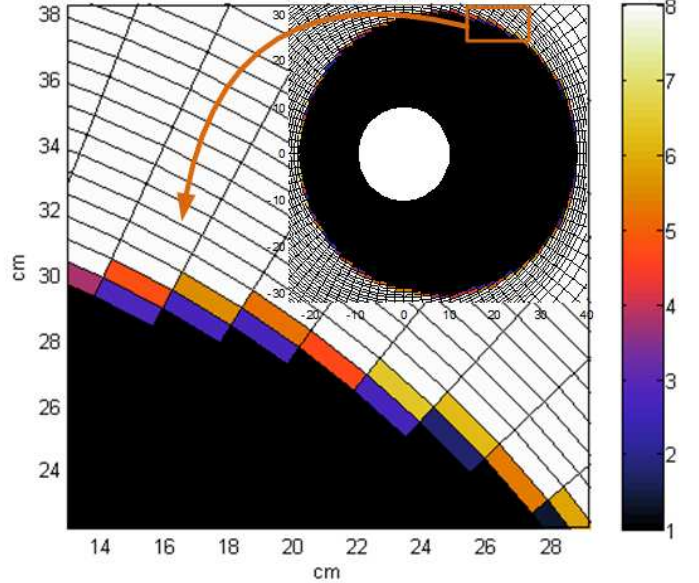


Fig. 4. Distribution of the cross-section effective conductivity $\sigma_{\phi\rho}^{eff}$ along the borehole/formation interface in the cylindrical FDTD grid representing the eccentered LWD sensor geometry.

and the eccentricity are equal to 12 inches and 3 inches, respectively. The discretization on the cross-section shown employs $(N_\rho, N_\phi) = (70, 100)$ grid points with $\Delta\rho = 0.635$ cm close to the eccentered interface.

C. Further modeling issues

Once the conductivity tensor is determined, the FDTD update equations for the electric \mathbf{E} and magnetic \mathbf{H} fields in anisotropic conductive media with tensor $\bar{\sigma}^a$ are written as in [17], with the effective conductivity elements above used to describe the tensor $\bar{\sigma}^a$ for grid elements along the eccentered borehole/formation interface. The 3-D cylindrical FDTD grid is conformal to both the steel mandrel and the loop antennas, so that no staircasing error is produced in the discretization of these objects. A 3-D unsplit perfectly matched layer (PML) in cylindrical coordinates [30] is used as an absorbing boundary condition to suppress outgoing waves and minimize spurious reflections from the outer grid boundaries. Along the radial direction, a small $\Delta\rho$ is used in the region close to the mandrel and around the borehole/formation interface to provide better accuracy. Non-uniform gridding is employed within the Earth formation with $\Delta\rho$ progressively enlarged away from the borehole (where the discretization is less critical). The maximum $\Delta\rho$ in the formation is determined from $\Delta\rho_{max} = \delta_{min}/6$, where δ_{min} is the smallest skin depth, which is associated with the largest conductivity in the formation [17]. The longitudinal and azimuthal directions are uniformly discretized with constant $\Delta\phi$ and Δz . A ramped-sine function as in [12] is used for the source excitation. The ramp is used to avoid DC offset and high-frequency contamination that otherwise would arise from the discontinuity of the sine function derivative at $t = 0$ [31]. Amplitude and phase data is obtained from the time-domain results using the time-to-frequency extraction

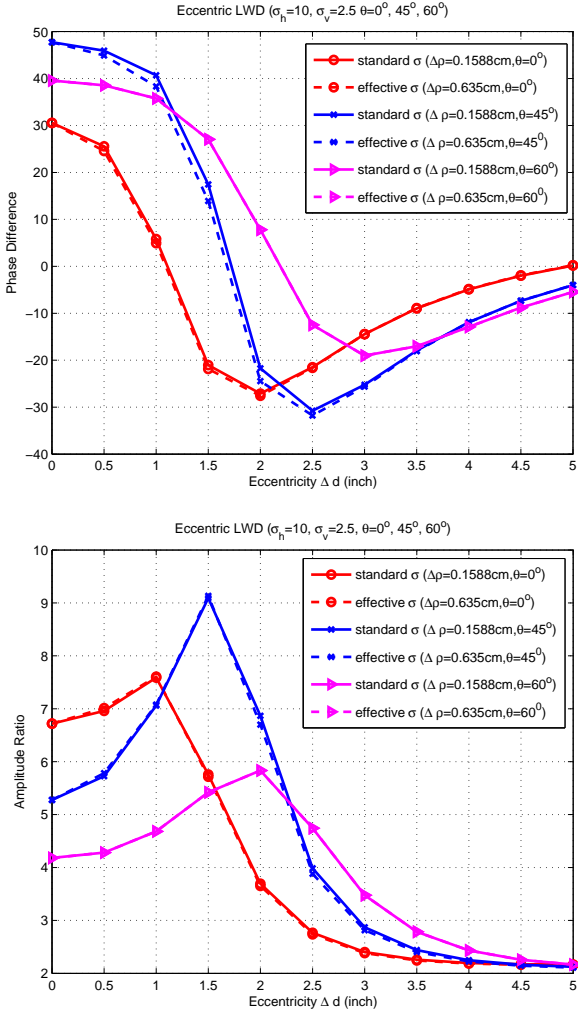


Fig. 5. Phase difference (top) and amplitude ratio (bottom) versus eccentricity offset Δd computed in a homogeneous anisotropic formation with $\sigma_h = 10$ S/m and $\sigma_v = 2.5$ S/m, for three dipping angles $\theta = 0^\circ, 45^\circ, 60^\circ$. The borehole radius is 12 inches.

algorithm described in [32].

III. NUMERICAL RESULTS

The sensor considered here is a prototypical LWD tool, as illustrated in Fig. 1. This sensor consisting of three loop antennas (one transmitter and two receivers) with 4.5 in radius, placed around a cylindrical steel mandrel with 4 in radius. The two receiver antennas are located at 30 and 24 in away from the transmitter, which operates at 2MHz. The steel mandrel is approximated as a perfect conductor, which is a good approximation at this operation frequency. The response of the LWD sensor consists of the phase difference and amplitude ratio between the voltages measured at the two receivers [17].

In all simulations described below, a uniform discretization is adopted for the z direction, with $\Delta z = 5.08$ cm. Furthermore, a cylindrical PML is employed with a cubic profile for the artificial PML conductivity along the ten outermost cells of the 3-D grid in the ρ and z directions.

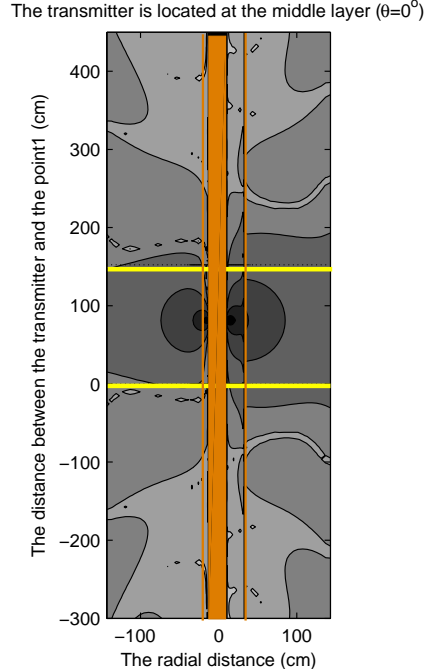


Fig. 6. Lateral cross-section of the field distribution produced by an eccentric LWD tool inside a three-layer formation. Because the fast decay in the field away from the transmitter, a warped logarithmic scale is used for visualization, with darker regions indicating stronger field. The parallel yellow lines indicate the mid bed. Two dipping angles are considered: $\theta = 0^\circ$ and $\theta = 45^\circ$. The borehole radii and eccentricity offset are equal to 9" and 3.5", respectively. The mid bed is anisotropic, with $\sigma_h = 0.01$ S/m and $\sigma_v = 0.005$ S/m. The top and bottom layers are both isotropic, with $\sigma_{iso} = 1$ S/m. The borehole (mud) conductivity is $\sigma_{mud} = 0.0005$ S/m. The transmitter is located in the mid layer, at the position distinguishable by large field magnitude. Two effects are visible from this qualitative plot: deeper radial field penetration into the mid bed due to lower conductivity (larger skin depth) and directional effect in azimuth due to tool/borehole eccentricity. A residual reflected field from the PML is visible, especially at the corners, but at a level much below that in the region of interest.

A. Homogeneous Anisotropic Formation

We first consider the response of an eccentered LWD sensor in an anisotropic homogeneous formation with $\sigma_h = 10$ S/m and $\sigma_v = 2.5$ S/m, for three dipping angles: $\theta = 0^\circ, 45^\circ$ and 60° , and various eccentricity offsets Δd . The radius of the borehole is $R = 12$ inches. The borehole mud conductivity is $\sigma_{mud} = 0.0005$ S/m. The cylindrical grid uses $(N_\rho, N_\phi, N_z) = (N_\rho, 200, 100)$ grid points, where N_ρ varies in the interval 122–136. The variation for N_ρ follows because a uniform $\Delta\rho_{min} = 0.635$ cm is used in the borehole region and in the eccentered borehole/formation interface, whereas for larger ρ , $\Delta\rho$ is gradually increased from 0.635 cm to 1.876 cm. As a consequence, geometries with a larger eccentricity offset require larger N_ρ .

Fig. 5 shows the phase difference and amplitude ratio for the dipping angles considered, as Δd is varied. The “effective σ ” curves refer to simulations using the discretization parameters above and employing effective conductivities at the borehole/formation interface. Also shown are results employing a finer grid in the radial direction (requiring about four times more radial nodes and computer memory) and where no effective conductivity is used (i.e., plain staircasing is employed instead). The two sets of results agree very well, showing that the use of effective conductivities is quite effective in reducing the required memory (and CPU time).

B. Layered Formations with Anisotropic Dipping Bed

Next, we consider the response of an eccentered LWD sensor in a 9-in radius borehole through a three-layer formation with an anisotropic dipping bed, as illustrated in Fig. 1. The mud conductivity is again $\sigma_{mud} = 0.0005$ S/m. The top and bottom layers have isotropic conductivity, with $\sigma_{iso} = 1$ S/m. The anisotropic dipping bed has a fixed “vertical thickness” (true vertical depth) of 60 inches along the sensor axis. Two different dipping angles are considered: $\theta = 0^\circ$ and $\theta = 45^\circ$. In the dipping bed, the horizontal conductivity is $\sigma_h = 0.01$ S/m and the vertical conductivity is $\sigma_v = 0.005$ S/m. The computational domain is discretized using $(N_\rho, N_\phi, N_z) = (N_\rho, 200, 180)$ grid points, where N_ρ is chosen in the interval 58 ~ 72 grid points. In the ρ direction, a uniform $\Delta\rho_{min} = 0.635$ cm is chosen across the borehole and borehole/formation interface and a non-uniform $\Delta\rho$ is chosen further into the Earth formation, gradually increasing from 0.635 cm to 5.9314 cm.

Fig. 6 is a qualitative contour plot depicting a log-scale distribution of the E_ϕ component along the lateral cross-section of the borehole and surrounding formation. The transmitter is located in the center of the anisotropic dipping bed. The eccentricity offset is $\Delta d = 3.5$ inches in this case and the cross-section shown is along the plane defined by the offset. The field distributions do not present rotational asymmetry for both $\theta = 0^\circ$ and $\theta = 45^\circ$ due to the eccentricity. Note that the resolution provided by the field is slightly greater along the azimuthal direction where the tool is in close proximity to the formation. Fig. 6 further illustrates the vertical asymmetry of the field distribution along the lateral plane due to the dipping bed.

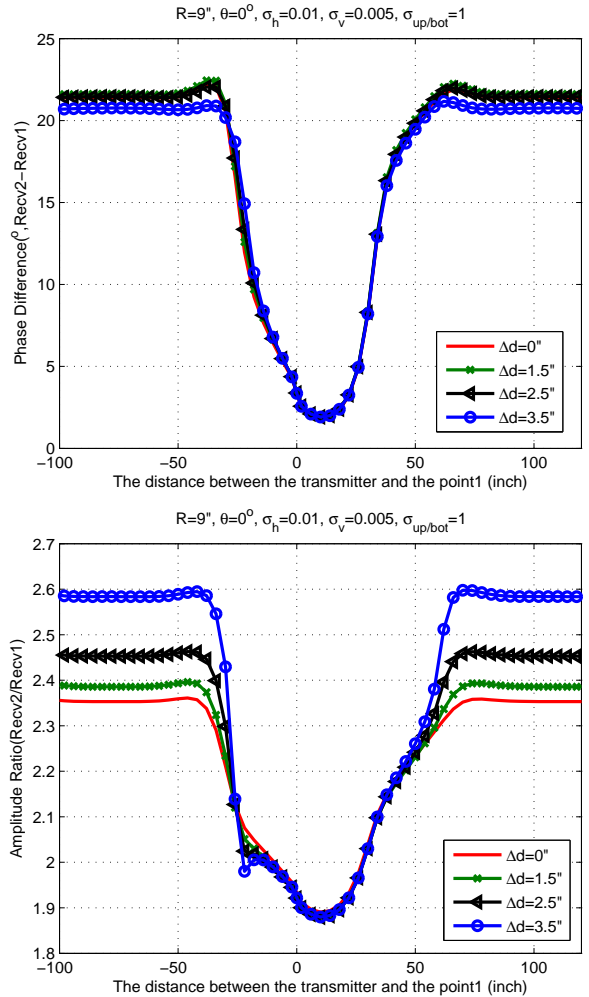


Fig. 7. Phase difference (top) and amplitude ratio (bottom) of the eccentered LWD sensor penetrating through an anisotropic dipping bed for different eccentricities. The borehole radius and eccentricity are equal to 9" and 3.5", respectively. The dipping angle is set up with $\theta = 0^\circ$. The anisotropic dipping bed has $\sigma_h = 0.01$ S/m and $\sigma_v = 0.005$ S/m. The top and bottom layers are equal to the isotropic conductivity of $\sigma_{iso} = 1$ S/m and the mud conductivity is $\sigma_{mud} = 0.0005$ S/m.

Fig. 7 and Fig. 8 show the phase difference and amplitude ratio between the voltage computed at the two receiver versus different eccentricity offsets Δd , for $\theta = 0^\circ$ and $\theta = 45^\circ$, respectively. For the case with $\theta = 0^\circ$, the tool is only sensitive to σ_h , and the response (in particular, the amplitude ratio) is more sensitive to the eccentricity offset in the top and bottom (isotropic) layers, where the contrast between the mud conductivity and the formation conductivity is higher. For the dipping case shown in Fig. 8, the response is sensitive to both σ_h and σ_v in the anisotropic bed. The higher sensitivity of the amplitude ratio response to the eccentricity offset in the top and bottom layers is again visible. Both the phase difference and the amplitude ratio show an increase in the apparent thickness of the dipping bed due to the slower transition of effective conductivities provided by such geometry (shoulder-bed effect). We stress that the same vertical thickness is used for both $\theta = 0^\circ$ and $\theta = 45^\circ$ cases. In the phase difference plot, one can also observe an increase in the “horn” effect for

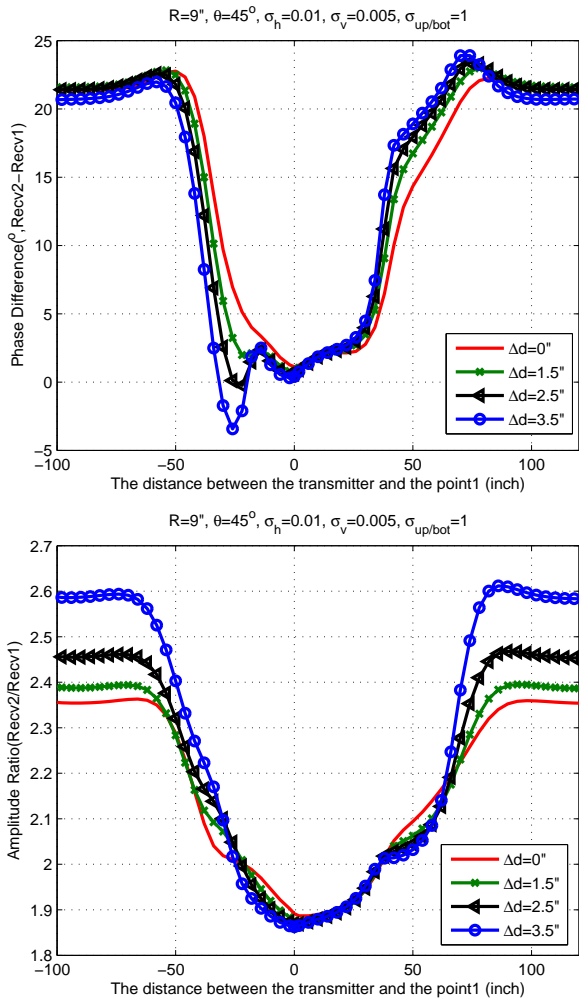


Fig. 8. Phase difference (top) and amplitude ratio (bottom) of the eccentered LWD sensor penetrating through an anisotropic dipping bed for different eccentricities. The borehole radius and eccentricity are equal to 9" and 3.5", respectively. The dipping angle is set up with $\theta = 45^\circ$. The anisotropic dipping bed has $\sigma_h = 0.01 \text{ S/m}$ and $\sigma_v = 0.005 \text{ S/m}$. The top and bottom layers are equal to the isotropic conductivity of $\sigma_{iso} = 1 \text{ S/m}$ and the mud conductivity is $\sigma_{mud} = 0.0005 \text{ S/m}$.

larger eccentricities.

Next we consider two fixed offsets, $\Delta d = 0$ and $\Delta d = 3.5$ inches, and examine the response for various dipping angles. In this example, instead of using a fixed true vertical depth for the mid bed, we use a fixed "actual thickness" (measured length) of 60 inches, see a graphical explanation of this terminology in [17]. Fig. 9 and Fig. 10 show a plot of the computed phase difference and amplitude ratio in this case. As the dipping angle is increased, the apparent thickness of the anisotropic dipping bed is widened due to the shoulder effect and the $\sec \theta$ geometrical factor present in the resulting vertical thickness. Fig. 10 shows once more that the eccentricity accentuates the horn effect seen in the phase difference response for larger dipping angles.

IV. CONCLUSION

A number of finite-difference models have been developed in the past for handling eccentered logging tools in isotropic

formations or centered logging tools in dipping anisotropic formations; however, none of those prior models were tailored for handling eccentered tools in dipping anisotropic formations. Here, we have described the numerical modeling of eccentered well-logging tools in dipping anisotropic Earth formations using a staggered-grid cylindrical 3-D FDTD algorithm with a leap-frog update that incorporates a locally-conformal technique to compute effective conductivities on partially-filled grid cells along the interface between the borehole and anisotropic formation without the need for excessive grid refinement. The algorithm was validated against results from conventional FDTD (with the latter employing a much finer grid), showing very good agreement. In particular, results for the phase difference and amplitude ratio of 2 MHz logging-while-drilling tool responses were found to be in good agreement even when using a radial cell size four times larger than conventional FDTD. Assuming uniform gridding along the radial direction, this would imply four-fold savings in memory versus conventional FDTD (in practice, the memory savings are somewhat smaller because non-uniform FDTD gridding can be deployed with larger cell sizes used away from the borehole boundary).

The proposed formulation was illustrated to compute the response of an eccentered LWD tool operating at 2 MHz in layered Earth formations with anisotropic dipping beds. For the combination of mud and formation conductivities considered here, the "horn" effect observed in dipping beds (particularly in the phase difference) was observed to be accentuated by the eccentricity offset. On the other hand, the latter has shown no discernible net effect on the "apparent" thickness of dipping beds.

REFERENCES

- [1] A. Q. Howard, Jr., "Petrophysics of magnetic dipole fields in an anisotropic earth," *IEEE Trans. Antennas Propag.*, vol. 48, no. 9, pp. 1376-1383, Sep. 2000.
- [2] J. H. Moran and S. Gianzero, "Effects of formation anisotropy on resistivity-logging measurements," *Geophys.*, vol. 44, no. 7, pp. 1266-1286, Jul. 1979.
- [3] C. J. Weiss and G. A. Newman, "Electromagnetic induction in a fully 3-D anisotropic earth," *Geophys.*, vol. 67, no. 4, pp. 1104-1114, 2002.
- [4] J. R. Lovell and W. C. Chew, "Effect of tool eccentricity on some electrical well-logging tools," *IEEE Trans. Geosci. Remote Sens.*, vol. 28, no. 1, pp. 127-136, Jan. 1990.
- [5] R. H. Hardman and L. C. Shen, "Theory of induction sonde in dipping beds," *Geophysics*, vol. 51, no. 3, pp. 800-809, Mar. 1986.
- [6] W. C. Chew, Z. Nie, Q. H. Liu, and B. Anderson, "An efficient solution for the response of electrical well logging tools in a complex environment," *IEEE Trans. Geosci. Remote Sens.*, vol. 29, no. 2, pp. 308-313, Mar. 1991.
- [7] J.-Q. He and Q. H. Liu, "A nonuniform cylindrical FDTD algorithm with improved PML and quasi-PML absorbing boundary conditions," *IEEE Trans. Geosci. Remote Sens.*, vol. 37, no. 2, pp. 1066-1072, Mar. 1999.
- [8] J. Li and C. Liu, "A three-dimensional transmission line method (TLM) for simulations of logging tools," *IEEE Trans. Geosci. Remote Sens.*, vol. 38, no. 4, pp. 1522-1529, Jul. 2000.
- [9] G.-X. Fan, Q. H. Liu, and S. P. Blanchard, "3-D numerical mode-matching (NMM) method for resistivity well-logging tools," *IEEE Trans. Geosci. Remote Sens.*, vol. 38, no. 10, pp. 1544-1552, Oct. 2000.
- [10] T. Wang and S. Fang, "3-D electromagnetic anisotropy modeling using finite-differences," *Geophys.*, vol. 66, no. 6, pp. 1386-1398, 2001.
- [11] S. Liu and M. Sato, "Electromagnetic logging technique based on borehole radar," *IEEE Trans. Geosci. Remote Sens.*, vol. 40, no. 9, pp. 2083-2092, Sep. 2002.

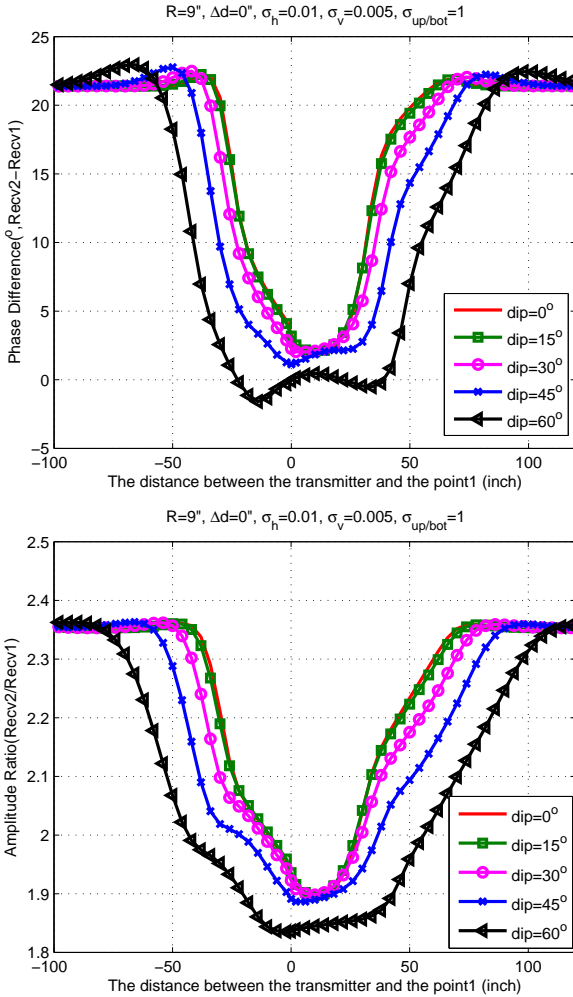


Fig. 9. Phase difference (top) and amplitude ratio (bottom) of the eccentered LWD sensor penetrating through an anisotropic dipping bed for various θ . The borehole radius and eccentricity are equal to 9" and 0", respectively. The anisotropic dipping bed has $\sigma_h = 0.01$ S/m and $\sigma_v = 0.005$ S/m. The top and bottom layers are equal to the isotropic conductivity of $\sigma_{iso} = 1$ S/m and the mud conductivity is set up with $\sigma_{mud} = 0.0005$ S/m.

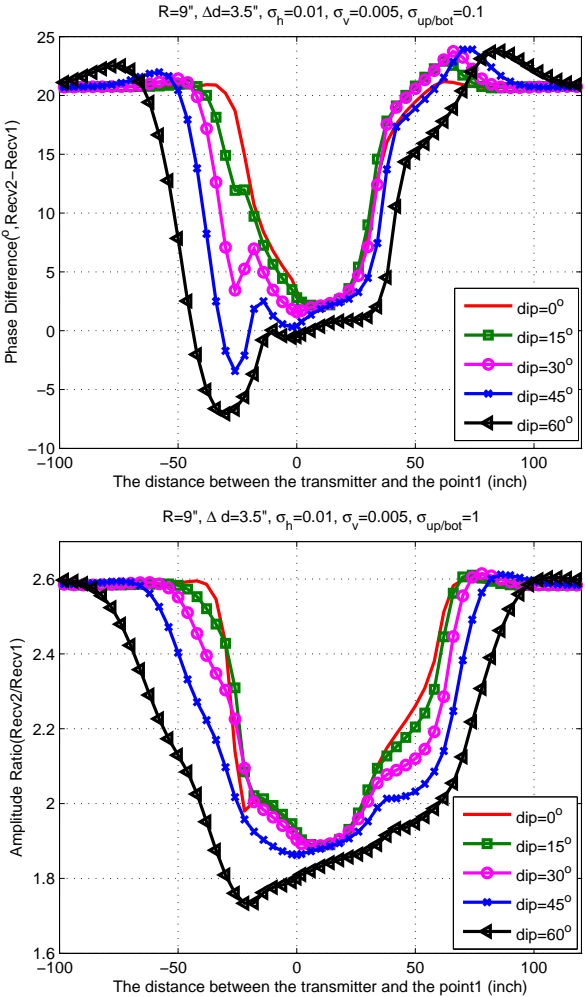


Fig. 10. Phase difference (top) and amplitude ratio (bottom) of the eccentered LWD sensor penetrating through an anisotropic dipping bed for various θ . The borehole radius and eccentricity are equal to 9" and 3.5", respectively. The anisotropic dipping bed has $\sigma_h = 0.01$ S/m and $\sigma_v = 0.005$ S/m. The top and bottom layers are equal to the isotropic conductivity of $\sigma_{iso} = 1$ S/m and the mud conductivity is set up with $\sigma_{mud} = 0.0005$ S/m.

- [12] Y.-K. Hue, F. L. Teixeira, L. E. San Martin, and M. Bittar, "Three-dimensional simulation of eccentric LWD tool response in boreholes through dipping formations," *IEEE Trans. Geosci. Remote Sens.*, vol. 43, no. 2, pp. 257-268, Feb. 2005.
- [13] G. Gao and C. Torres-Verdin, "Efficient numerical simulation of axisymmetric electromagnetic induction measurements using a high-order generalized extended Born approximation," *IEEE Trans. Geosci. Remote Sens.*, vol. 44, no. 9, pp. 2445-2453, Sep. 2006.
- [14] Y.-K. Hue and F. L. Teixeira, "Analysis of tilted-coil eccentric borehole antennas in cylindrical multilayered formations for well-logging applications," *IEEE Trans. Antennas Propag.*, vol. 54, no. 4, pp. 1058-1064, Apr. 2006.
- [15] G. Xing and S. Yang, "The response functions of electromagnetic wave logs and their applications," *IEEE Trans. Geosci. Remote Sens.*, vol. 44, no. 6, pp. 1413-1418, Jun. 2006.
- [16] Y.-K. Hue and F. L. Teixeira, "Numerical mode-matching method for tilted-coil antennas in cylindrically layered anisotropic media with multiple horizontal beds," *IEEE Trans. Geosci. Remote Sens.*, vol. 45, no. 8, pp. 2451-2462, Aug. 2007.
- [17] H.-O. Lee and F. L. Teixeira, "Cylindrical FDTD analysis of LWD tools through anisotropic dipping-layered Earth media," *IEEE Trans. Geosci. Remote Sens.*, vol. 45, no. 2, pp. 383-388, Feb. 2007.
- [18] D. Wu, C.R. Liu, and J. Chen, "An efficient FDTD method for axially symmetric LWD environments," *IEEE Trans. Geosci. Remote Sens.*, vol. 46, no. 6, pp. 1652-1656, Jun. 2008.
- [19] D. Pardo, C. Torres-Verdin, M. J. Nama, M. Paszynski, and V. M. Calo, "Fourier series expansion in a non-orthogonal system of coordinates for the simulation of 3D alternating current borehole resistivity measurements," *Comput. Methods Appl. Mech. Engrg.*, vol. 197, pp. 3836-3849, 2008.
- [20] L. Zhong, A. Bhardwaj, L. C. Shen, and R. C. Liu, "Computation of triaxial induction logging tools in layered anisotropic dipping formations," *IEEE Trans. Geosci. Remote Sens.*, vol. 46, no. 4, pp. 1148-1163, Apr. 2008.
- [21] S. Ebihara and Y. Inoue, "Analysis of eccentered dipole antenna for borehole radar," *IEEE Trans. Geosci. Remote Sens.*, vol. 47, no. 4, pp. 1073-1088, Apr. 2009.
- [22] M. S. Novo, L. C. da Silva, and F. L. Teixeira, "Three-dimensional finite-volume analysis of directional resistivity logging sensors," *IEEE Trans. Geosci. Remote Sens.*, vol. 48, no. 3, pp. 1151-1158, 2010.
- [23] S. Davydychova, "Separation of azimuthal effects for new generation resistivity logging tools – Part I," *Geophys.*, vol. 75, no. 1, pp. E31-E40, 2010.
- [24] M. S. Novo, F. L. Teixeira, and L. C. da Silva, "Three-dimensional finite-volume analysis of directional resistivity logging sensors," *IEEE Trans. Geosci. Remote Sens.*, vol. 48, no. 3, pp. 1151-1158, Mar. 2010.
- [25] A. Taflove and S. Hagness, *Computational Electrodynamics: The Finite Difference Time-Domain Method*, 3rd. edition, Boston, Mass.: Artech House, 2005.
- [26] W. Yu and R. Mittra, "A conformal finite-difference time-domain

- technique for modeling curved dielectric surfaces," *IEEE Microwave Wireless Compon. Lett.*, vol. 11, no. 1, pp. 25-27, Feb. 2005.
- [27] N. Kaneda, B. Houshmand, and T. Itoh, "FDTD analysis of dielectric resonators with curved surfaces," *IEEE Trans. Microwave Theory Tech.*, vol. 11, no. 1, pp. 25-27, Feb. 2005.
- [28] K.-P. Hwang and A. C. Cangellaris, "Effective permittivities for second-order accurate FDTD equations at dielectric interfaces," *IEEE Microwave Wireless Compon. Lett.*, vol. 11, no. 4, pp. 158-160, Feb. 2001.
- [29] H.-O. Lee and F. L. Teixeira, "Locally-conformal FDTD for anisotropic conductive interfaces," *IEEE Trans. Antennas Propag.*, vol. 58, no. 11, pp. 3658-3664, 2010.
- [30] F. L. Teixeira and W. C. Chew, "Finite-difference computation of transient electromagnetic waves for cylindrical geometries in complex media," *IEEE Trans. Geosci. Remote Sens.*, vol. 38, no. 4, pp. 1530-1543, Jul. 2000.
- [31] C. M. Furse, D. H. Roper and D. N. Buechler, "The problem and treatment of DC offsets in FDTD simulations," *IEEE Trans. Antennas Propag.*, vol. 48, no. 8, pp. 1198-1201, Aug. 2000.
- [32] C. M. Furse, "Faster than Fourier: Ultra-efficient time to frequency-domain conversions for FDTD simulations," *IEEE Trans. Antennas Propag. Mag.*, vol. 42, no. 6, pp. 24-34, Dec. 2000.

Dr. Bittar is a Senior Director of Technology for Middle East and North Africa for Halliburton in Dhahran Saudi Arabia. He joined Halliburton through Sperry-Sun Drilling Services in 1990 and since then has held various technical and leadership roles, including Halliburton Technology Fellow and Senior Director of Formation Evaluation. Dr. Bittar has contributed to the advancement of logging while drilling (LWD), wireline resistivity, and logging sensor technology and interpretation. He received the Society of Petrophysicists and Well Log Analysts (SPWLA) Technical Achievement Award in 2006 and currently serves on King Abdullah University of Science and Technology (KAUST) Industry Advisory Board.

Hwa-Ok Lee received the M.S. degree in Electrical Engineering from The Ohio State University, Columbus, in 2005, where she is currently working toward the Ph.D. degree, also in Electrical Engineering.

Her current research interests include computational electromagnetics and numerical analysis of resistivity logging tools.

Fernando L. Teixeira received the Ph.D degree in Electrical Engineering from the University of Illinois at Urbana-Champaign in 1999. From 1999 to 2000 he was a Postdoctoral Associate with the Massachusetts Institute of Technology. In 2000 he joined the The Ohio State University, where he is now a Professor with the Department of Electrical and Computer Engineering and also affiliated with the ElectroScience Laboratory.

His current research interests include modeling of electromagnetic sensors for hydrocarbon exploration, time-domain computational electromagnetics, metamaterials, and ultrawideband inverse scattering. Dr. Teixeira received a number of awards for his research, including the CAREER Award from the National Science Foundation, the triennial Booker Fellowship from the International Union of Radio Science (USNC/URSI), and the Outstanding Young Engineer Award from the IEEE Microwave Society (MTT-S). He has served as chair of the Joint IEEE AP/MTT-S Columbus Chapter and currently serves as Associate Editor for the IEEE Antennas and Wireless Propagation Letters.

Luis E. San Martin received the Ph.D. degree in Physics from the University of Illinois at Urbana-Champaign, in 1998.

After graduation, he joined Halliburton Energy Services Research in Houston, Texas. He is currently a Principal Scientist with the Sensor Physics Department at Halliburton, as part of the Electromagnetic Group. Dr. San Martin has a number of publications and patents in the areas of data analysis and design of well-logging tools for hydrocarbon exploration.

Michael S. Bittar received his B.S., M.S. and Ph.D. degrees, all in Electrical Engineering, from the University of Houston, Houston, TX in 1983, 1986 and 1990, respectively.